JOURNAL OF MATERIALS SCIENCE 32 (1997) 5445–5455

Elastic moduli and damage evolution of three-axis woven fabric composites

WEN-SHYONG KUO*, BIN-JEN PON
Department of Textile Engineering, Feng Chia University, Taichung, Taiwan

Three-axis orthogonal woven fabric composites composed of carbon fibres and epoxy resin have been fabricated. Examined from micrographs, the fabric weaving yarns were found to be very slender with aspect ratios ranging from 11–13.6. Based upon the observed geometry, the composite has been modelled by a unit cell comprising wavy yarns. Both elliptical and lenticular cross-sections were adopted to simulate the slender weaving yarns. Taking into account one-dimensional stress concentration and yarn undulation, an iso-phase approach has been developed to analyse the composite elastic moduli. A higher weaving yarn aspect ratio was found to result in a lower modulus. Modulus reduction due to yarn undulation was more significant in weaving directions. Material characterization has been conducted based upon monotonic tensile and three-point flexural tests, and detailed damage mechanisms for both loadings have been examined. The onset of damage under tensile loading was found to be *z*-axis yarn debonding, followed by debonding and splitting in *y*-axis yarns. When subjected to flexural loading, yarn debonding, transverse cracking, and interyarn matrix cracking were the dominant damage mechanisms which appeared on specimen tensile sides. Stress transfer among yarns and how it relates to the composite damage have been discussed in detail.

1. Introduction

Three-dimensional textile composites are a unique class of materials, produced by impregnating matrix materials into fabric preforms to hold multidirectional yarns together. According to fabricating techniques, three-dimensional preforms are usually categorized into the following groups: woven, braided, stitched, and knitted [1]. Among them, woven and braided fabrics can possess a relatively high fraction of reinforcing fibres in the out-of-plane direction and from a major portion of high-performance three-dimensional textile composites [1, 2]. In comparison with two-dimensional laminated structures, textile composites based on three-dimensional preforms offer unique transverse properties. As a result of through-the-thickness reinforcing fibres, the composite transverse properties (including strength, stiffness, and fracture toughness) can be effectively enhanced. Because these composites are essentially free from delamination and edge effects, which are often serious problems in laminated composites [3, 4], they are suitable for multidirectional load-bearing applications. Another attractive feature is the ability to formulate directly three-dimensional near-net-shape fabrics. With this feature, joining and machining problems could be eliminated, and thus a better structural integrity can be achieved.

Compared with laminated composites, three-dimensional textile composites are significantly more complex in design and analysis due to spatial and inhomogeneous fabric structures. Besides those related to fibre matrix microstructures, parameters involved in designing three-dimensional textile composites include yarn size, yarn orientation, and interlacing patterns. Thus, it is often difficult to determine analytically the material behaviour and to optimize the composites through the control of these parameters.

In analysing elastic behaviour of the composites, several approaches have been proposed. The simplest method is probably the so-called aggregate model, assuming that the composite stiffness is the sum of each constituent stiffness weighted by its volume fraction [5–8]. This model is a consequence of the assumption that the strains are independent of positions [8]. As a result, strain concentrations due to fabric architecture are smeared out. In practice, this model would be suitable for fabrics with sufficient amount of fibres in all three axes. In dealing with these complex-geometry and multi-material problems, numerical approaches, such as finite element methods, have proven to be useful [8–11]. Another promising approach is the three-dimensional consistent higher-order theory [12], using the concept of minimum potential energies and Lagrange multipliers to ensure stress equilibrium across dissimilar materials. However, these numerical methods inevitably require a large number of nodal points and a large increase in computational time to obtain satisfactory three-dimensional stress and strain

* Author to whom all correspondence should be addressed.

0022–2461 © *1997 Chapman & Hall*

distributions. A simple means able to address this problem in an elasticity consistent manner is unlikely to exist. Based on the iso-phase model developed for two-dimensional woven fabric composites [8, 13, 14], the elastic moduli of the three-dimensional composites with wavy yarns are analysed in this paper.

Owing to fabric architecture, complicated damage mechanisms and significant non-linearity can be expected for the composites [15, 16]. Understanding the onset and development of damage requires the knowledge of defects caused during material processing and stress concentrations due to material inhomogeneity. Yarn interfacial defects caused by incomplete wetting are especially important because yarn debonding, which is analogous to delamination in laminated composites, is one of the principal fracture mechanisms in the early stage of damage accumulation. Besides yarn debonding, subcritical damage in the composites includes interyarn matrix cracking, yarn splitting, and fibre breakages associated with yarn abrasion. These subcritical damage mechanisms generally occur at a level much lower than ultimate strains, resulting in a stiffness reduction and, possibly, an opening of direct paths for environmental attack on fibres. Although these mechanisms might contribute to an increase in composite toughness, the associated shortcomings can adversely affect the resulting stiffness and strength and limit the usefulness of the composites. Thus, the goal of this work was to provide experimentally validated information on the composite damage evolution, with particular emphasis on the interrelationship between processing, microstructure, and fracture behaviour.

2. Experimental procedure

The fibre system used was high-tenacity carbon fibres with 12K tow roving manufactured by Toho company. The fibre diameter, strength, and longitudinal modulus are 7 μm, 2800 MPa, and 232 GPa, respectively. By using a three-dimensional weaving loom, fabrics with various weaving patterns can be fabricated. Examined in this paper is a three-axis orthogonal woven fabric composite. In this paper, axial yarns are selected to be parallel to the z-axis, and the weaving yarns are oriented in x and y directions. The axial yarns consist of two tows of fibres (24K), and the weaving yarns are of one tow (12K). A beating process has been applied to weaving yarns in each weaving cycle to enhance fibre content.

The woven fabrics were then infiltrated by epoxy resin using a resin transfer moulding technique, followed by a curing process to consolidate the composites. The epoxy resin system used was GY260 DGEBA-type by Ciba-Geigy; the curing and toughening agents were HT976 and Der732, respectively. The Young's modulus and Poisson's ratio of the epoxy are 3.5 GPa and 0.35, respectively. The consolidated composites were then machined to desired dimensions for testing specimens. During machining, the interlacing loops on composite surfaces have been removed.

For tensile specimens, the nominal length, width, and thickness were 200, 20 and 3 mm, respectively. Glass-epoxy tabs with a length of 40 mm were adhesively bonded on both ends of the specimens. Specimen surfaces were polished to reduce damage during machining and to facilitate microscopic observations for damage evolution. Because the composite is macroscopically inhomogeneous, an extensometer, instead of a strain gauge that measures strains in a much smaller region, was used to obtain the average composite strains. The nominal specimen dimensions for three-point bending tests were 80, 20 and 3.1 mm, and the span length was 65 mm. Detailed dimensions for each specimen have been measured for the calculation of material moduli. Six specimens were prepared for each test, and the crosshead speed was 1 mm min^{-1}.

3. Fabric geometry

The woven preform examined in this paper is a three-axis orthogonal fabric. The basic fabric structure is shown in Fig. 1a with all yarns being straight. The axial yarns, or so-called through-the-thickness yarns, are selected in parallel with the z-axis, and the xy-plane, where the weaving yarns lay, is termed the weaving plane.

According to microscopic observations, yarn undulation takes place in almost all yarns that are designed to be straight. The following reasons may be the

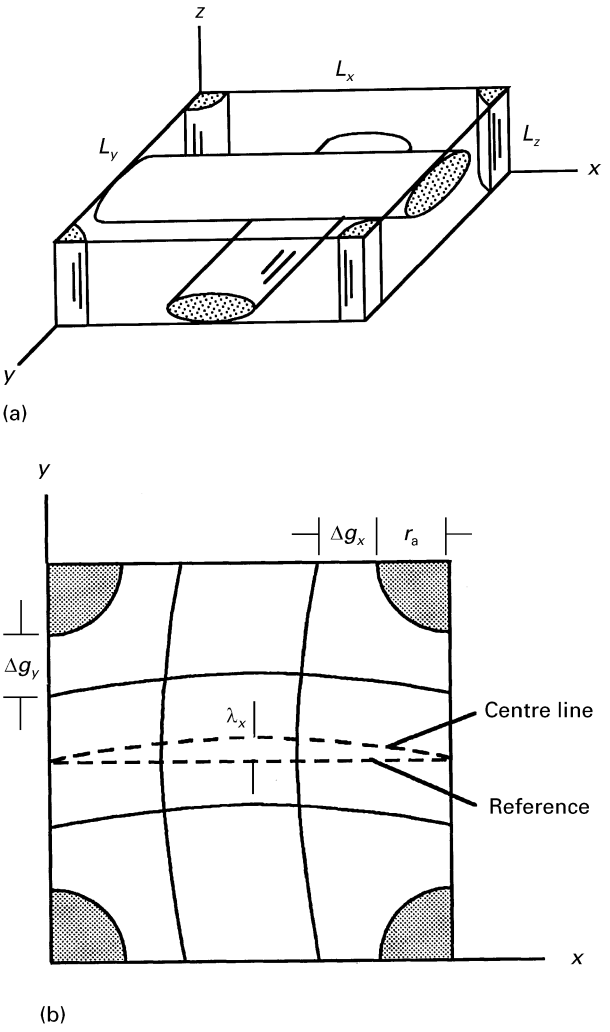

Figure 1 Unit cell for the three-axis fabric: (a) straight yarns, (b) wavy yarns with $n_x = 1$, $n_y = 1$.

causes for yarn distortion. First, yarn jam and distortion often occur in fabrics especially for those having high fibre content. For the fabricated preform in which the fibre content in weaving yarns is much higher than that in axial yarns, even a slight yarn jam in between axial and weaving yarns can induce a sufficient lateral force to cause axial yarn distortion. Second, because preforms should eventually be unmounted from the weaving loom before performing resin transfer moulding and curing, tensions in axial yarns, that keep the yarn straight, no longer exist and yarn undulation can be exacerbated. The third reason is the beating process, which is necessary to enhance preform compactness, upon weaving yarns. This causes distortion in the weaving yarns. Weaving yarn cross-sectional shapes, as will be discussed, are also dominated by this process. Another reason is the driving force for resin to impregnate into preforms. Flexible yarns can be deformed, especially when resin viscosity is high and a high driving force is necessary.

Realistic simulation of observed spatial yarn undulation is not easy, and thus a simple model is adopted. Fig. 1b shows the unit cell for yarn undulation. The unit cell dimensions are denoted as L_x, L_y, and L_z. Although the shapes are inherently irregular, the influence of the undulation on composite behaviour could be examined by assuming sinuous wave functions with amplitude λ_x, λ_y, and λ_z, respectively, for x-, y-, and z-axis yarns. To simplify the analysis, the wavelengths are limited to be $2L_x/n_x$, $2L_y/n_y$, and $2L_z/n_z$, where n_x, n_y, and n_z are integers. For example, the centre-line of the x-axis yarn on the weaving plane is described by

$$y = \lambda_x \sin\left(\frac{n_x \pi x}{L_x}\right) + y_0 \tag{1}$$

where y_0 is a constant for a relative position. The angle between the centre-line and the x-axis is

$$\theta_x = \tan^{-1}\left[\frac{n_x \pi \lambda_x}{L_x} \cos\left(\frac{n_x \pi x}{L_x}\right)\right] \tag{2}$$

Compared with the lengthwise distortion, cross-sections of weaving yarns are predictable. Fig. 2 is a micrograph showing weaving yarn cross-sections. Having been squeezed during the beating process, weaving yarns are slender and close to elliptical or lenticular shapes with aspect ratios ranging from 11–13.6. On the other hand, axial yarn cross-sections are irregular, and no single shape is representative.

In this paper, the axial yarn cross-section is assumed to be circular with radius r_a as shown in Fig. 1b. The weaving yarns are either elliptical or lenticular with major and minor semiaxes being r_{w1} and r_{w2}, respectively (Fig. 3). In this paper, the lenticular shape is defined to consist of two symmetric parabolic curves. The gaps between axial and weaving yarns are Δg_x and Δg_y. When yarn waviness is small, yarn lengths and hence yarn volume fractions can be obtained by neglecting higher order terms as

$$Y_x = \frac{A_{x0}}{L_y L_z}\left[1 + \left(\frac{\pi n_x \lambda_x}{2L_x}\right)^2\right] \tag{3a}$$

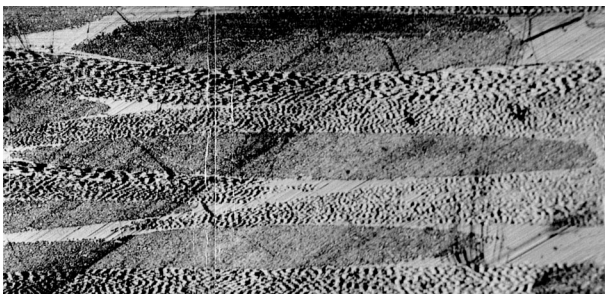

Figure 2 Micrograph showing slender weaving yarns.

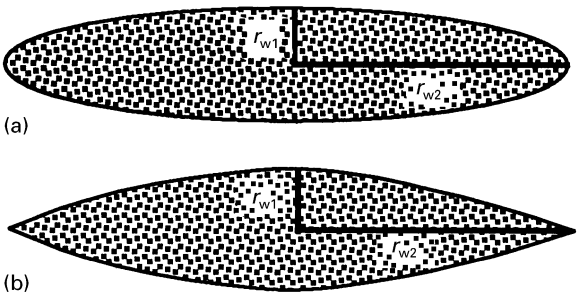

Figure 3 Shapes to model weaving yarns: (a) elliptical, (b) lenticular.

$$Y_y = \frac{A_{y0}}{L_x L_z}\left[1 + \left(\frac{\pi n_y \lambda_y}{2L_y}\right)^2\right] \tag{3b}$$

$$Y_z = \frac{A_{z0}}{L_x L_y}\left[1 + \left(\frac{\pi n_z \lambda_z}{2L_z}\right)^2\right] \tag{3c}$$

where A_{i0} is the cross-sectional area normal to the centre-line of the i-axis yarn defined as

$$A_{x0} = A_{y0} = \begin{cases} \pi r_{w1} r_{w2} & \text{elliptical} \\ \frac{8}{3} r_{w1} r_{w2} & \text{lenticular} \end{cases} \tag{4a}$$

$$A_{z0} = \pi r_a^2 \tag{4b}$$

From Fig. 1b, the unit-cell dimensions are $L_x = 2r_a + 2r_{w1}\ (1 + 2\bar{\lambda}_x) + 2\Delta g_x$, $L_y = 2r_a + 2r_{w1}\ (1 + 2\bar{\lambda}_y) + 2\Delta g_y$, and $L_z = 4r_{w2}$. It should be noted that the yarn spacings L_x and L_y are generally controllable and can serve as designing variables. On the other hand, L_z, as dominated by yarn size and squeezing pressure, could not be changed freely in a controlled manner, and thus should be measured from experiments; similar conclusions can be drawn for r_{w1}, r_{w2}, Δg_x, and Δg_y.

The total yarn volume fraction, denoted Y, is the sum of the volume fraction of each yarn. The space not occupied by yarn is termed the interyarn space, which is supposed to be filled by matrix materials. The matrix in this space is termed the interyarn matrix. Consequently, the interyarn matrix volume fraction, V_{im}, is equal to $1 - Y$ if the interyarn space is void-free.

4. Three-dimensional transformations

In this paper, the (1,2,3) system is termed on material coordinate to relate the local principal material directions; and the (x, y, z) system is termed the geometrical coordinate to refer to the global system. To represent a spatial orientation, three linearly independent

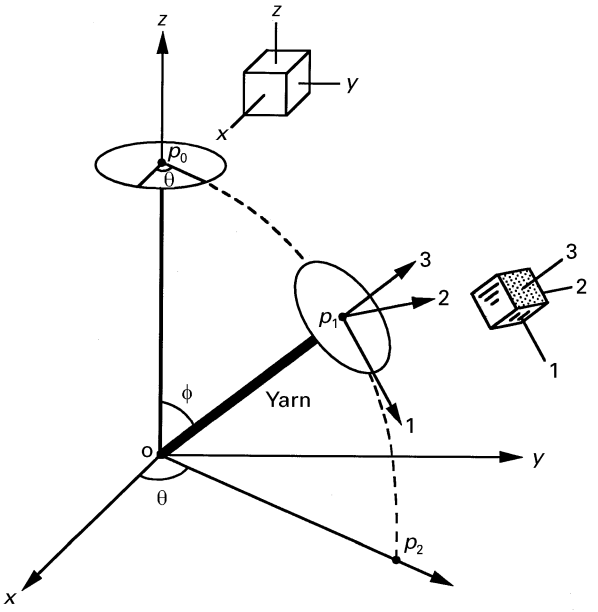

Figure 4 Three-dimensional rotation of a spatially oriented yarn.

rotational vectors are generally required. Yarns comprising fibres and matrix are very close to transversely isotropic, because fibres are generally uniform within yarns. Therefore, if axis 3 is designated to be the fibre direction, the material is then isotropic on the 12-plane. As a result, the rotation with respect to axis 3 is irrelevant to the resulting yarn properties, and thus two angles (θ, ϕ) are enough to represent a yarn rotation as shown in Fig. 4.

Let $\mathbf{u}_1$, $\mathbf{u}_2$ and $\mathbf{u}_3$ be the unit vectors in the (1,2,3) coordinate and $\mathbf{u}_x$, $\mathbf{u}_y$ and $\mathbf{u}_z$ be the unit vectors in the (x, y, z) coordinate. The relations between these two sets of vectors can be expressed as

$$\begin{bmatrix} \mathbf{u}_x \\ \mathbf{u}_y \\ \mathbf{u}_z \end{bmatrix} = \begin{bmatrix} mp & -n & mq \\ np & m & nq \\ -q & 0 & p \end{bmatrix} \begin{bmatrix} \mathbf{u}_1 \\ \mathbf{u}_2 \\ \mathbf{u}_3 \end{bmatrix} \tag{5}$$

where $m = \cos(\theta)$, $n = \sin(\theta)$, $p = \cos(\phi)$, and $q = \sin(\phi)$.

Let us denote [**Q**] as the stiffness matrix to relate the stress and engineering strain vectors in the 1–2–3 system. Because both stress and strain are second-order tensors, the transformation between these two coordinates can be readily obtained using tensor transformation laws. Thus, the transformed stiffness matrix for the x–y–z system can be proven to be [17]

$$[\bar{\mathbf{Q}}] = [\mathbf{T}]^{-1}[\mathbf{Q}][\mathbf{R}][\mathbf{T}][\mathbf{R}]^{-1} \tag{6}$$

where [**T**] is the stress transformation matrix as listed in the Appendix A.1, and [**R**] is a 6-by-6 diagonal matrix with the diagonal terms being {1,1,1,2,2,2}. All matrices in Equations 2 and 3 are of 6-by-6. Unless otherwise noted, the barred symbols refer to the x–y–z systems. Equation 6 can be evaluated easily based upon numerical computation. However, closed-form solutions for a transversely isotropic material have been obtained as listed in the Appendix A.2.

5. Three-dimensional elasticity analysis

Owing to yarn architecture and material inhomogeneity, the stress and strain distributions in the composites should be three-dimensional. The complexity of three-dimensional precludes simple solutions satisfying all required conditions from the elasticity point of view. Therefore, simplification on the deformation relations must be made in order that theoretical analysis can be performed. For example, the aggregate model, the most popular approach to evaluate the elastic constants for complex three-dimensional composites, assumes that the strains are constants throughout a composite. Obviously, this model can be inaccurate when strain concentration is significant.

The concept of the iso-phase mode originally developed by the author for two-dimensional woven ceramic-matrix composites [8], is extended herein for the three-dimensional problems. The composite is first modelled by a unit cell, and strains within the unit cell are assumed to be one-dimensional. Force equilibrium is then used to evaluate the strain functions, which enable composite deformation to be obtained. In comparison with the traditional iso-strain or rule-of-mixture approaches, this model takes into account one-dimensional stress/strain concentrations. Physically this model is an improvement although the significance of this improvement depends on fabric geometries and fibre content [8].

The unit-cell deformations are assumed to be functions of the associated directions, i.e. $u_x(x)$, $u_y(y)$, and $u_z(z)$. The normal strains are therefore one-dimensional, i.e. $\varepsilon_x(x)$, $\varepsilon_y(y)$, and $\varepsilon_z(z)$. The Poisson's effects are taken into account in an average manner, and the normal-shear coupling is neglected. Based upon these assumptions, the stress–strain relations become [8, 17]

$$\sigma_{xx}^{(k)}(x, y, z) = \bar{Q}_{11}^{(k)}\varepsilon_x(x) + \bar{Q}_{12}^{(k)}\bar{\varepsilon}_y + \bar{Q}_{13}^{(k)}\bar{\varepsilon}_z \tag{7a}$$

$$\sigma_{yy}^{(k)}(x, y, z) = \bar{Q}_{12}^{(k)}\bar{\varepsilon}_x + \bar{Q}_{22}^{(k)}\varepsilon_y(y) + \bar{Q}_{23}^{(k)}\bar{\varepsilon}_z \tag{7b}$$

$$\sigma_{zz}^{(k)}(x, y, z) = \bar{Q}_{13}^{(k)}\bar{\varepsilon}_x + \bar{Q}_{23}^{(k)}\bar{\varepsilon}_y + \bar{Q}_{33}^{(k)}\varepsilon_z(z) \tag{7c}$$

where the superscript (k) is an index for material constituent elements. For the fabric studied, there are four constituent elements: x-, y-, and z-axis yarns, and interyarn matrix. The $\bar{Q}_{ij}^{(k)}$ are the reduced stiffness of the kth constituent element with respect to the x–y–z coordinate. The barred strains stand for average values defined as

$$\bar{\varepsilon}_x = \frac{1}{L_x}\int_0^{L_x} \varepsilon_x(x)\,\mathrm{d}x \tag{8a}$$

$$\bar{\varepsilon}_y = \frac{1}{L_y}\int_0^{L_y} \varepsilon_y(y)\,\mathrm{d}y \tag{8b}$$

$$\bar{\varepsilon}_z = \frac{1}{L_z}\int_0^{L_z} \varepsilon_z(z)\,\mathrm{d}z \tag{8c}$$

where L_x, L_y, and L_z are the unit-cell dimensions. Defining F_{ij} as the resultant force component acting on a cross-section perpendicular to the i-axis in the direction of the j-axis, the resultant normal force is equal to the summation of the force component in

each constituent element within a cross-section

$$F_{xx} = \sum_k A_x^{(k)}(x)\sigma_{xx}^{(k)}(x) \tag{9a}$$

$$F_{yy} = \sum_k A_y^{(k)}(y)\sigma_{yy}^{(k)}(y) \tag{9b}$$

$$F_{zz} = \sum_k A_z^{(k)}(z)\sigma_{zz}^{(k)}(z) \tag{9c}$$

where $A_x^{(k)}(x)$, $A_y^{(k)}(y)$ and $A_z^{(k)}(z)$ are the areas of the kth constituent element in cross-sections normal to the x, y and z directions, respectively. For example, for a straight y-axis yarn with elliptical cross section, the area functions are

$$A_x^{(2)}(x) = \begin{cases} 2L_y r_{w2}\left[1 - \left(\dfrac{x - L_x/2}{r_{w1}}\right)^2\right]^{1/2} \\ \qquad -r_{w1} \leqslant x - L_x/2 \leqslant r_{w1} \\ 0 \quad \text{otherwise} \end{cases} \tag{10a}$$

$$A_y^{(2)}(y) = \pi r_{w1} r_{w2} \tag{10b}$$

$$A_z^{(2)}(z) = \begin{cases} 2L_y r_{w1}\left[1 - \left(\dfrac{z - r_{w2}}{r_{w2}}\right)^2\right]^{1/2} & 0 \leqslant z \leqslant 2r_{w2} \\ 0 & \text{otherwise} \end{cases} \tag{10c}$$

where the superscript (2) is the number to represent the y-axis yarn. The closed-form area functions become tedious if the yarn is wavy ($\lambda_y \neq 0$). However, their numerical values can be readily obtained.

The areas and stresses in Equations 9a–c are functions of location. However, the forces F_{ij} should remain constant due to force equilibrium. Substituting Equations 7a–c into Equations 9a–c, the relations between $\varepsilon_x(x)$ and F_{xx} can be recast as follows

$$\varepsilon_x(x) = \frac{F_{xx} - \sum_k A_x^{(k)}(x)[\bar{Q}_{12}^{(k)}\bar{\varepsilon}_y - \bar{Q}_{13}^{(k)}\bar{\varepsilon}_z]}{\sum_k A_x^{(k)}(x)\bar{Q}_{11}^{(k)}} \tag{11}$$

The resultant forces must be in equilibrium with externally applied forces. Therefore

$$F_{xx} = L_y L_z \sigma_{xx}^{\infty} \tag{12}$$

where the σ_{xx}^{∞} is an externally applied stress at far-field. Averaging the strains according to Equation 11 and using Equation 12, the relation between σ_{xx}^{∞} and the average strains is obtained. Applying the same procedure for σ_{yy}^{∞} and σ_{zz}^{∞}, the following relations can be obtained

$$\begin{bmatrix} \sigma_{xx}^{\infty} \\ \sigma_{yy}^{\infty} \\ \sigma_{zz}^{\infty} \end{bmatrix} = \begin{bmatrix} Q_{11}^{c} & Q_{12}^{c} & Q_{13}^{c} \\ Q_{21}^{c} & Q_{22}^{c} & Q_{23}^{c} \\ Q_{31}^{c} & Q_{32}^{c} & Q_{33}^{c} \end{bmatrix} \begin{bmatrix} \bar{\varepsilon}_x \\ \bar{\varepsilon}_y \\ \bar{\varepsilon}_z \end{bmatrix} \tag{13}$$

where the superscript c in the stiffness matrix stands for composite. The detailed expressions for Q_{ij}^{c} are listed as follows

$$Q_{1j}^{c} = \int_0^{L_x} \frac{\sum_k A_x^{(k)}(x)\bar{Q}_{1j}^{(k)}}{\sum_k A_x^{(k)}(x)\bar{Q}_{11}^{(k)}}\,dx \left[\int_0^{L_x} \frac{L_y L_z}{\sum_k A_x^{(k)}(x)\bar{Q}_{11}^{(k)}}\,dx\right]^{-1} \tag{14a}$$

$$Q_{2j}^{c} = \int_0^{L_y} \frac{\sum_k A_y^{(k)}(y)\bar{Q}_{2j}^{(k)}}{\sum_k A_y^{(k)}(y)\bar{Q}_{22}^{(k)}}\,dy \left[\int_0^{L_y} \frac{L_x L_z}{\sum_k A_y^{(k)}(y)\bar{Q}_{22}^{(k)}}\,dy\right]^{-1} \tag{14b}$$

$$Q_{3j}^{c} = \int_0^{L_z} \frac{\sum_k A_z^{(k)}(z)\bar{Q}_{3j}^{(k)}}{\sum_k A_z^{(k)}(z)\bar{Q}_{33}^{(k)}}\,dz \left[\int_0^{L_z} \frac{L_x L_y}{\sum_k A_z^{(k)}(z)\bar{Q}_{33}^{(k)}}\,dz\right]^{-1} \tag{14c}$$

where j is an index ranging from 1–3, and k is the material index ranging from 1 to the number of constituent elements. It should be noted that the stiffness matrix Q_{ij}^{c} is not explicitly symmetric as required by the reciprocal relation. This is due to the assumption of the stress and strain relation (Equation 7) which is a simplification for this three-dimensionally inhomogeneous problem. According to numerical examinations, the discrepancy between Q_{ij}^{c} and Q_{ji}^{c} is generally very small, and the diagonal terms in the stiffness matrix are much larger than the off-diagonal ones, reducing the influence of the discrepancy on composite elastic properties.

The inverse of the stiffness matrix in Equation 13 yields the corresponding compliance matrix $[\mathbf{S}^{c}]$, from which the composite elastic moduli can be obtained

$$E_x = \frac{1}{S_{11}^{c}} \tag{15a}$$

$$E_y = \frac{1}{S_{22}^{c}} \tag{15b}$$

$$E_z = \frac{1}{S_{33}^{c}} \tag{15c}$$

The composite Poisson's ratios can also be obtained from the same compliance matrix. To analyse composite shear moduli, however, requires re-examination on the composite deformation relations (Equation 7) under shear forces, which is not discussed in this paper.

6. Results and discussion

6.1. Experimental results

The fibre volume fractions of the yarns are calculated based upon the fibre diameter (7 μm), the yarn sizes (12K for weaving yarns, 24K for axial yarns), and the measured yarn shapes. The measured weaving yarn widths ($2r_{w1}$) were 3.1–3.8 mm, and the average value of the weaving yarn thickness ($2r_{w2}$) was 0.28 mm. Thus the aspect ratios are 11–13.6. For the fabricated composite, the unit-cell dimensions L_x and L_y are both 8 mm, and L_z ($4r_{w2}$) is 0.56 mm. The calculated fibre volume fractions in the x-, y-, and z-axis are 10.3%, 10.3%, and 1.4%, respectively; the overall fibre volume fraction is 22%. The fibre volume fraction within a yarn depends on the yarn cross-sectional area. The calculated fibre volume fractions within the weaving yarn are listed in Table I as a function of yarn aspect ratio and yarn shape. With identical aspect ratio, a lenticular shape is smaller and hence fibre packing is denser.

Three typical stress–strain curves (a–c) for the composite subjected to monotonically increasing uniaxial tensile loads are shown in Fig. 5. The curves can be roughly divided into three stages. Stage I is the initial linear portion of the curves; no major damage has

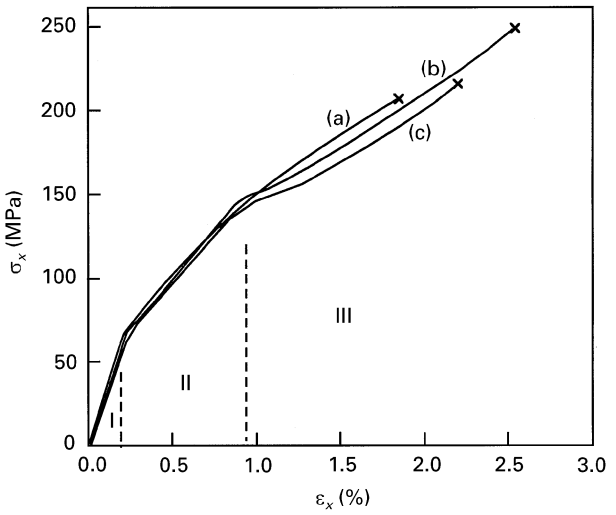

Figure 5 Stress–strain relations for tensile tests.

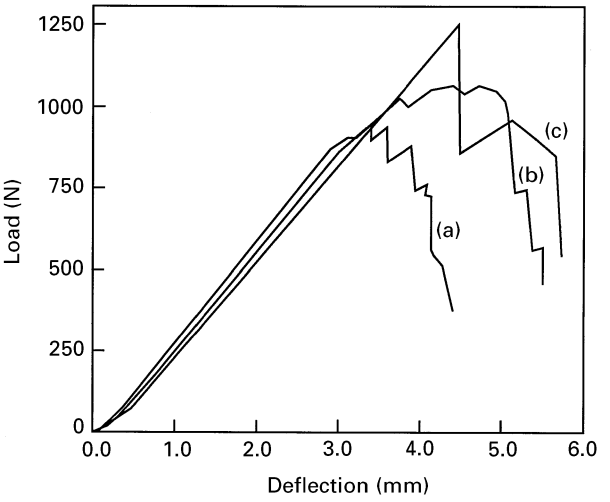

Figure 6 Load–deflection relations for flexural tests.

been found on specimen surfaces. The first deviation from linearity occurs at a strain about 0.2%, followed by another linear portion with reduced slope indicated as Stage II. The second deviation from linearity occurs at a strain about 0.9%. Toward the higher stress and the slope is further decreased, and the stress–strain curve shows slight upward convexity. The measured values for the composite modulus from the slopes in Stage I were 27.4–31.9 GPa.

Three typical load–deflection relations (a–c) for three-point flexure tests are shown in Fig. 6. A rather low slope has been found at the early stage of loading. As the load increases, the material appears to behave linearly almost up to its ultimate load, beyond which the load drops drastically with a saw-like curve. The measured ultimate loads were 940–1250 N, and the measured flexure modulus based upon the linear portion of the curves were 29.8–34.9 GPa.

6.2. Analysis of elastic modulus

Elastic properties of yarns are the essential information in predicting the overall composite properties. Based upon the fibre and matrix properties and the calculated fibre volume fractions as listed in Table I, four yarn elastic constants (E_1, E_3, G_{13}, and ν_{13}) are estimated by simple rule-of-mixture as listed in Appendix A.3, and the Poisson's ratio in the isotropic plane ν_{12}, due to the lack of a well-defined rule, is assumed to be 0.3. With these constants, the 6-by-6 [**Q**] matrix can be easily obtained. The rotational angles (θ, ϕ) for straight x-, y-, and z-axis yarns are $(0°, 90°)$, $(90°, 90°)$, and $(0°, 0°)$, respectively. Composite stiffness elements and moduli are evaluated according to Equations 14 and 15 with varying yarn aspect ratio, yarn shape, and undulation amplitude.

The predicted Young's modulus, E_x, is shown in Fig. 7 for the case $\lambda_x = \lambda_y$, $\lambda_z = 0$, and $n_x = n_y = 1$. Within the measured range of the aspect ratio (11.0–13.6), the modulus predicted by assuming a lenticular cross-section is slightly higher than that predicted by elliptical cross-section. With the weaving yarn thickness fixed, the modulus slightly decreases as the aspect ratio of weaving yarn increases, indicating

TABLE I Fibre volume fractions in weaving yarns (r_{w2} = 0.14 mm)

Aspect ratio	Elliptical	Lenticular
11	0.682	0.803
12	0.625	0.736
13	0.577	0.679
14	0.536	0.631

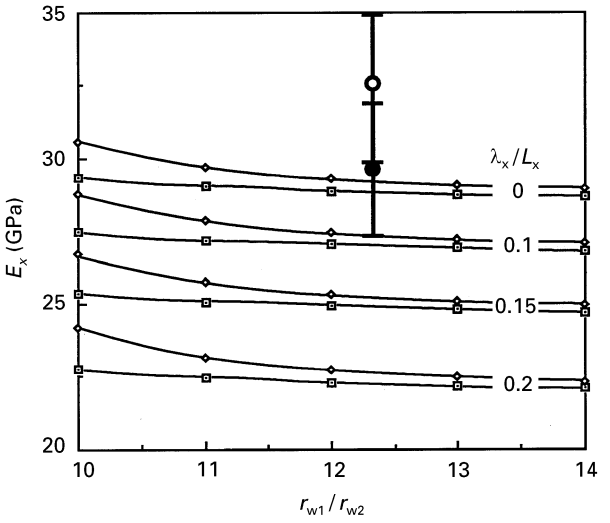

Figure 7 Predicted composite modulus, E_x, as a function of weaving yarn shape; (●) solid, (◇) lenticular, (□) elliptical. Average tensile modulus, (○) average flexural modulus.

that the variation in weaving yarn width does not significantly affect the modulus. Owing to the irregular nature of yarn geometries, accurately quantitative measurements of yarn wavinesses require statistical approaches. According to micrographs, waving amplitude up to 20% of yarn spacing is likely to occur in fabrics. Therefore, the effect of yarn waviness is illustrated with $\lambda_x/L_x = 0-0.2$, and because E_x is insensitive to z-axis yarns, z-axis yarns are assumed to be straight. As shown in Figs 7 and 8, the modulus reduction rate increases with the waviness. As the yarn waviness does not exceed $\lambda_x/L_x = 0.05$, the modulus is

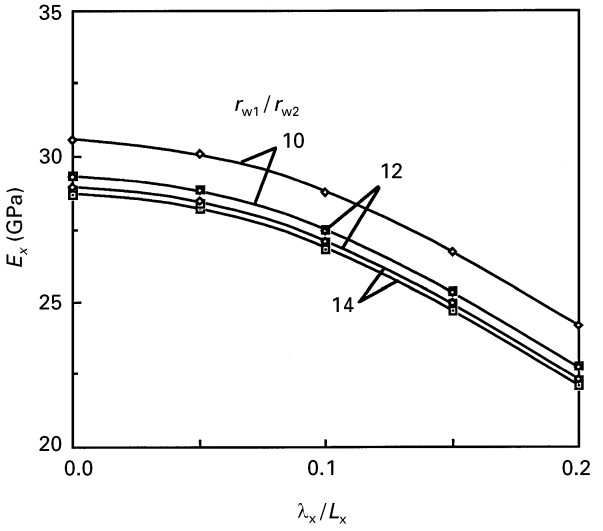

Figure 8 Predicted composite modulus, E_x, as a function of weaving yarn waviness. (◇) Lenticular, (□) elliptical.

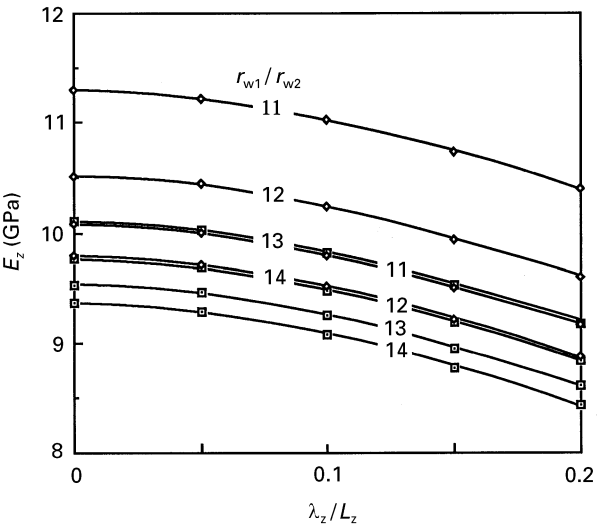

Figure 9 Predicted composite modulus, E_z, as a function of weaving yarn shape. (◇) Lenticular, (□) elliptical.

insensitive to the waviness. It is noted that the stiffness reduction due to the off-axis of yarns is less prominent than that of an angle-ply in a laminate, because yarn undulation also results in a volume increase as revealed in Equation 3. The ranges and average values from both tests are indicated with the solid and open circles representing tensile and flexural moduli, respectively. The predicted range for E_x is found to be lower than the experimental ranges. The source data of fibre modulus, fibre diameter, and yarn thickness are crucial to the predicted results. Along with the fibre and yarn data, relative high scatter in experimental results is a problem requiring re-examination, as will be discussed in Section 6.6.

Fig. 9 shows the variation of the transverse modulus, E_z, with respect to the waviness of z-axis yarns and the aspect ratio of weaving yarns, assuming $\lambda_x = \lambda_y = 0$ and $n_z = 1$. While E_x is dominated solely by x-axis yarns, all yarns are important to E_z because fibre content in the z-axis is rather low (1.4%). Thus, the reduction of E_z due to z-axis yarn undulation is less significant than that of E_x due to x-axis yarn undulation (Fig. 8).

It must again be stated that the theoretical modelling work is based on the premises that fibre/matrix and yarn/matrix interfacial bondings are perfect, and the composite is damage- and void-free. Analyses of the influence of these factors in practical textile composites might require knowledge of manufacturing processes and would not be fully understood without a micromechanics approach focusing on the interyarn and intrayarn levels.

6.3. Stress transfer and characteristics lengths

Stress transfer within yarns and the interyarn matrix is essential for understanding composite damage mechanisms. When the specimen is subjected to a uniaxial load, forces are transferred from end tabs to the interior through the action of shear stresses. The shear stresses gradually turn into normal stresses in the middle (test section) of the specimen. For macroscopically homogeneous materials, shear stresses should vanish in the test section where stresses reach a steady-state. However, for the three-dimensional composite discussed, the material is macroscopically inhomogeneous, and the interfacial shear stresses between yarns and the interyarn matrix should exist in the test section. Thus, the normal stresses in yarns are not invariable even when subjected to a uniaxial tension.

Load transfer within the composite can be divided into macroscopic and microscopic levels. Stress transfer between yarns and the interyarn matrix is on a macroscopic level, focusing on the interactions between yarns. Stress transfer between fibres and matrix in a yarn is microscopic. The characteristics of these stress-transfer mechanisms can be very different, and the composite damage is dependent on these characteristics. One important parameter to characterize stress transferring is characteristic length, defined as the length required for stresses to reach a steady state. The characteristic length depends on the material modulus, geometrical shape, and, more importantly, interfacial properties. At the macroscopic level, yarns are usually treated as homogeneous bodies, and the yarn characteristic length is a few times the yarn thickness or width [18]. Damage mechanisms, such as yarn transverse cracking, yarn debonding, and yarn pull-out, depend very much on this length. On the other hand, the characteristic length for the stress transfer within a fibre is a few fibre diameters, which is much shorter than the yarn characteristic length. This fibre characteristic length is important to microscopic damage such as fibre breakage, fibre debonding, and fibre pull-out. Microscopic analysis of the damage within a yarn is somehow similar to that in a unidirectional composite, which has been well documented in the literature. Therefore, this research focuses on the yarn damage rather than microscopic damage within the fibre/matrix levels.

6.4. Damage due to tensile loading

The composite is virtually identical in the x and y directions. In the case studied, the loading is selected to be parallel to the x-axis yarns as shown in Fig. 10a. As stresses are transferred among dissimilar components, stress concentrations often occur at interfaces between yarns and the interyarn matrix. According to microscopic observation, cracks were found to initiate at the interfaces of z-axis yarns in a form of yarn/matrix debonding, which could be responsible for the first deviation from linearity.

The debonded z-axis yarns can be located on the edges or inside the specimen. It was found that those z-axis yarns located on specimen edges were likely to debond earlier than those inside the specimen, leaving empty notches as shown in Figs 10b and 11. Two reasons may account for this. First, the yarns on the edge can be damaged during specimen-edge machining. Second, stresses in the interface of a z-axis yarn on the edge are unbalanced, because one side of the yarn is free from stresses. During application of the load, some of these yarns were found to pop-out from specimen edges. On the other hand, for those inside the specimen, the yarns are constrained and are less likely to debond earlier than those on edges. Therefore, the first damage mode tends to be the debonding of z-axis yarns on specimen edges, followed by the debonding of z-axis yarns inside specimens.

As the applied load increases, debonding and splitting in y-axis yarns occur as shown in Figs 10c, 10d and 12. Both fracture modes can be termed transverse cracking, analogous to that in laminated composites. The propagation of these cracks will be hindered by the strong fibres in the x-axis yarns. The creation of these transverse cracks depends upon the flaws on the interface or within the y-axis yarns. Once a transverse crack forms, the stresses inside the yarn are significantly changed due to the creation of free surfaces, thus imparting loads to neighbouring x-axis yarns. This stress redistribution reduces the possibility for another parallel crack to occur in the cracked yarn. The number of transverse cracks within a yarn depends on the loading level and the yarn characteristic length discussed in the previous section.

The densities of debonding in z-axis yarns and cracking in y-axis yarns increase with the applied load, creating more stress concentrations for x-axis yarns. The development of the damage reduces the contribution of the y- and z-axis yarns to the composite stiffness, as shown in the significant non-linearity of the stress–strain curves. The correlation between the amount of damage and the non-linearity needs further investigation from both material characterization and fracture analysis.

Because the majority of the load is carried by x-axis yarns, the final composite failure is therefore determined by these yarns. The sudden drop of the curve beyond the ultimate point suggests that x-axis yarns are brittle and the propagation of yarn fracture is unstable. Fig. 13 shows a specimen fractured due to tensile loading. The separations of the z-axis yarns and surrounding resin from the specimen create empty holes. Crack propagation in x-axis yarns was found to traverse the yarns; very little yarn brushing has been observed.

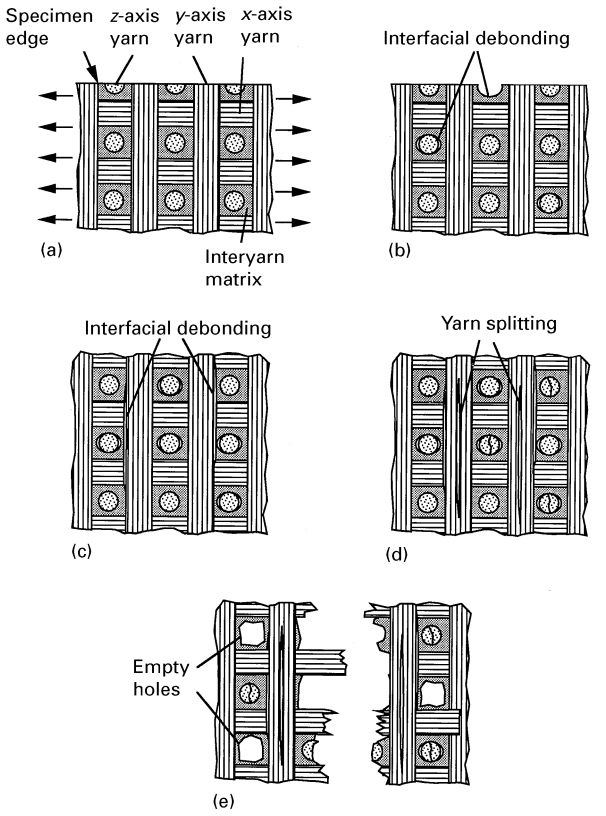

Figure 10 Schematic drawing of damage evolution due to tensile loading.

Figure 11 Edge notches due to debonding in the z-axis yarns.

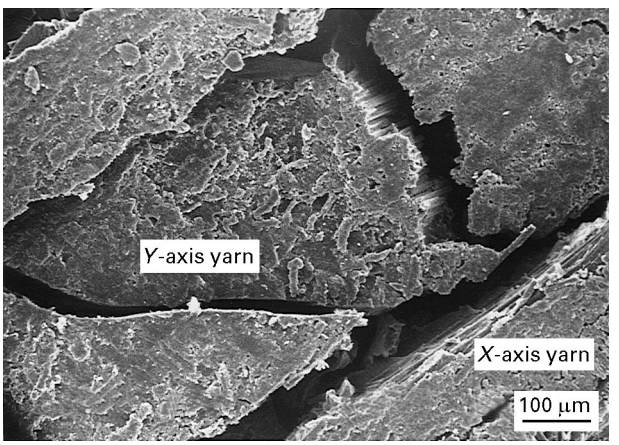

Figure 12 Transverse cracks in a y-axis yarn.

6.5. Damage due to flexural loading

As shown in Fig. 6, slightly upward convexity occurs at the beginning of loading; no clear indication of damage has been found at this level. This feature, which is not found in uniaxial tensile tests, could be related to (1) the material deformation at the points where the flexural load is applied, (2) the realignment of undulated yarns, and (3) the closure of pre-existing microcracks in the compressive (upper) part of the specimen, resulting in an increased stiffness. The onset of damage was found at the central region of the bottom side in a combination of debonding in the z-axis yarns, transverse cracking in y-axis yarns, and interyarn matrix cracking. The appearance of these modes depends on yarn location. Fig. 14 shows transverse cracking in a y-axis yarn that was located at the centre of the bottom surface.

The sharp drop in load, followed by a saw-like curve, is associated with the tensile rupture in x-axis yarns together with yarn peeling from the surface. Yarn rupture and peeling proceed progressively from the bottom towards the top surface, resulting in a zigzag fracture path observed from specimen edges, as shown in Fig. 15a. This zigzag crack propagation can be altered by z-axis yarns having weak interfaces, resulting in the crack being deviated into an upward direction along a debonded z-axis yarn interface (Fig. 15b). It is therefore noted that although the presence of z-axis yarns can enhance transverse properties, which has been emphasized as the major advantage of three-dimensional composites, attention should be paid to the created z-axis yarn interface and the associated interfacial failure, which could involve opening through-the-thickness cracks and cause unexpected problems [15].

6.6. Material inhomogeneity and related problems

It should be noted that the damage mechanisms discussed were based upon the micrographs taken from composite surfaces, and whether surface fracture morphology is representative of the damage inside the composite is an important issue to pursue, especially for inhomogeneous materials. Attention should also be paid to the design of specimen dimensions for experimental characterization. Compared to laminates, material characterization standards for three-dimensional textile composites are less-well defined. For example, a narrow specimen should be inappropriate for the three-dimensional fabric composite having large yarn spacing, because specimens with identical sizes could contain uneven sets of x-axis yarns. This can cause scattering in material characterization and result in dissimilar damage mechanisms. Using wider specimens or cutting specimens with identical relative position from composites would be helpful for this, although practical limitations may exist. Another feasible approach is to fabricate near-net-shape fabrics designed for specimens [19]. The advantages are obvious: (1) specimens are identical in yarn content, (2) specimen machining and induced material degradation can be eliminated, and (3) surface loops can be retained to delineate better the three-dimensional composites in practical applications.

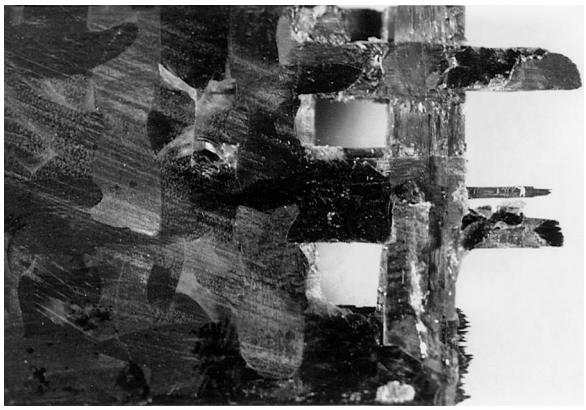

Figure 13 A specimen fractured due to tensile loading.

Figure 14 Cracks on the tensile side due to flexural loading.

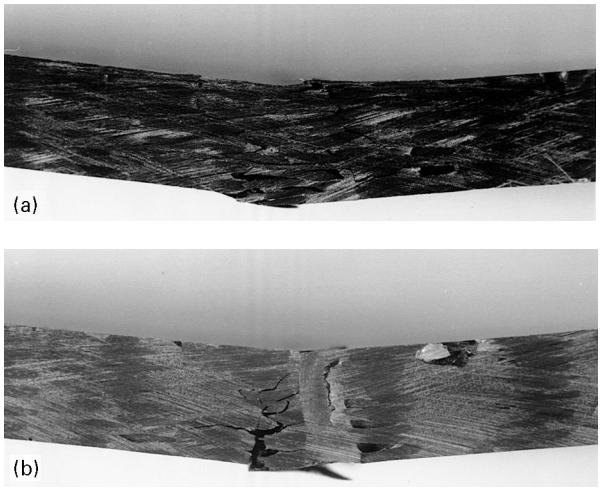

Figure 15 Crack propagation due to flexural loading.

7. Conclusions

The moduli E_x and E_z predicted by assuming a lenticular shape are higher than those predicted by an elliptical shape with identical aspect ratio. Within the measured range for the weaving yarn aspect ratios (11–13.6), the moduli are slightly decreased with the

ratio. Causes for yarn undulation during composite fabrication have been discussed, and the influence of yarn undulation on the moduli has been numerically examined. Because x-axis yarns possess higher fibre volume fraction, E_x is more sensitive to yarn undulation. Damage mechanisms have been investigated based upon tensile and flexural tests. Interfacial debonding of z-axis yarns is found to be dominant for crack initiation in tensile tests. Debonding and splitting in y-axis yarns are followed. These subcritical types of damage are responsible for the non-linearity in the stress–strain curves. The composite catastrophic failure is associated with the brittle fracture in x-yarns. In contrast to tensile tests, the onset of damage under flexural loading consists of various mechanisms, including debonding in z-axis yarns, transverse cracking in y-axis yarns, and interyarn matrix cracking. The rupture and peeling of x-axis yarns develop successively from the bottom towards the top surface, resulting in a zigzag fracture path and a saw-like load–deflection response. The stress transfer and material inhomogeneity that are closely related to the damage mechanisms of the composites are also discussed.

Acknowledgements

The authors thank the Department of Textile Engineering, Feng Chia University, and the National Science Council of Taiwan, for the support of this research (NSC 85-2216-E-035-012).

Appendix

A.1. Stress transformation matrix [T] and $[\mathbf{T}]^{-1}$

$$[\mathbf{T}] = \begin{bmatrix} m^2p^2 & n^2p^2 & q^2 & -2npq & -2mpq & 2mnp^2 \\ n^2 & m^2 & 0 & 0 & 0 & -2mn \\ m^2q^2 & n^2q^2 & p^2 & 2npq & 2mpq & 2mnq^2 \\ -mnq & mnq & 0 & mp & -np & m^2q - n^2q \\ m^2pq & n^2pq & -pq & np^2 - nq^2 & mp^2 - mq^2 & 2mnpq \\ -mnp & mnp & 0 & -mq & nq & pm^2 - pn^2 \end{bmatrix} \tag{A1}$$

$$[\mathbf{T}]^{-1} = \begin{bmatrix} m^2p^2 & n^2 & m^2q^2 & -2mnq & 2m^2pq & -2mnp \\ n^2p^2 & m^2 & n^2q^2 & 2mnq & 2n^2pq & 2mnp \\ q^2 & 0 & p^2 & 0 & -2pq & 0 \\ -npq & 0 & npq & mp & np^2 - nq^2 & -mq \\ -mpq & 0 & mpq & -np & mp^2 - mq^2 & nq \\ mnp^2 & -mn & mnq^2 & m^2q - n^2q & 2mnpq & pm^2 - pn^2 \end{bmatrix} \tag{A2}$$

A.2. Stiffness transformation for a transversely isotropic material

If axis 3 is designated to be the axis of symmetry, the material is then isotropic on the 12-plane, resulting in the following relations

$$Q_{11} = Q_{22} \tag{A3a}$$

$$Q_{13} = Q_{23} \tag{A3b}$$

$$Q_{44} = Q_{55} \tag{A3c}$$

$$Q_{66} = \frac{1}{2}(Q_{11} - Q_{12}) \tag{A3d}$$

Using these relations, the resulting transformations from Equation 6 can be proven to be

$$\bar{Q}_{11} = Q_{11}(m^2p^2 + n^2) + Q_{33}m^2q^2 - K_0m^2q^2(m^2p^2 + n^2) \tag{A4a}$$

$$\bar{Q}_{12} = Q_{12}p^2 + Q_{13}q^2 + K_0q^4m^2n^2 \tag{A4b}$$

$$\bar{Q}_{13} = Q_{12}n^2q^2 + Q_{13}(n^2p^2 + m^2) + K_0m^2p^2q^2 \tag{A4c}$$

$$\bar{Q}_{14} = npq(Q_{13} - Q_{12} + K_0m^2q^2) \tag{A4d}$$

$$\bar{Q}_{15} = mnq(Q_{13} - Q_{11} + 2Q_{55} + K_0m^2q^2) \tag{A4e}$$

$$\bar{Q}_{16} = mnq^2(Q_{13} - Q_{11} + 2Q_{55} + K_0m^2q^2) \tag{A4f}$$

$$\bar{Q}_{22} = Q_{11}(n^2p^2 + m^2) + Q_{33}n^2q^2 - K_0n^2q^2(n^2p^2 + m^2) \tag{A4g}$$

$$\bar{Q}_{23} = Q_{12}m^2q^2 + Q_{13}(m^2p^2 + n^2) + K_0n^2p^2q^2 \tag{A4h}$$

$$\bar{Q}_{24} = npq(Q_{13} - Q_{11} + 2Q_{55} + K_0n^2q^2) \tag{A4i}$$

$$\bar{Q}_{25} = mpq(Q_{13} - Q_{12} + K_0n^2q^2) \tag{A4j}$$

$$\bar{Q}_{26} = mnq^2(Q_{13} - Q_{11} + 2Q_{55} + K_0n^2q^2) \tag{A4k}$$

$$\bar{Q}_{33} = Q_{11}q^2 + Q_{33}p^2 - K_0p^2q^2 \tag{A4l}$$

$$\bar{Q}_{34} = npq(Q_{13} - Q_{11} + 2Q_{55} + K_0p^2) \tag{A4m}$$

$$\bar{Q}_{35} = mpq(Q_{13} - Q_{11} + 2Q_{55} + K_0p^2) \tag{A4n}$$

$$\bar{Q}_{36} = mnq^2(Q_{13} - Q_{12} + K_0p^2) \tag{A4o}$$

$$\bar{Q}_{44} = Q_{55}(m^2p^2 + n^2) + Q_{66}m^2q^2 + K_0n^2p^2q^2 \tag{A4p}$$

$$\bar{Q}_{45} = mnq^2(Q_{55} - Q_{66} + K_0p^2) \tag{A4q}$$

$$\bar{Q}_{46} = mpq(Q_{55} - Q_{66} + K_0n^2p^2) \tag{A4r}$$

$$\bar{Q}_{55} = Q_{55}(n^2p^2 + m^2) + Q_{66}n^2q^2 + K_0m^2p^2q^2 \tag{A4s}$$

$$\bar{Q}_{56} = npq(Q_{55} - Q_{66} + K_0m^2q^2) \tag{A4t}$$

$$\bar{Q}_{66} = Q_{55}q^2 + Q_{66}p^2 + K_0m^2n^2q^4 \tag{A4u}$$

where K_0 is a parameter for transversely isotropic materials defined as

$$K_0 = Q_{11} + Q_{33} - 2Q_{13} - 4Q_{55} \tag{A5}$$

It is noted that $K_0 = 0$ when the material is isotropic, and hence K_0 might be interpreted as a deviation from an isotropic medium.

A.3. Simple rule-of-mixture to predict yarn properties

$$E_1 = E_2 = \left(\frac{V_f}{E_f} + \frac{V_m}{E_m}\right)^{-1} \tag{A6a}$$

$$E_3 = E_f V_f + E_m V_m \tag{A6b}$$

$$\nu_{31} = \nu_{32} = \nu_f V_f + \nu_m V_m \tag{A6c}$$

$$G_{13} = G_{23} = \left(\frac{V_f}{G_f} + \frac{V_m}{G_m}\right)^{-1} \tag{A6d}$$

References

1. F. K. KO, in "Textile Structural Composites" edited by T. W. Chou and F. K. Ko (Elsevier, New York, 1989) p. 129.
2. B. Z. JANG, M. CHOLAKARA, B. P. JANG and W. K. SHIH, *Polymer Eng. Sci.* **31** (1991) 40.
3. K. DRANSFIELD, C. BAILLIE and Y. W. MAI, *Compos. Sci. Technol.* **50** (1994) 305.
4. D. LIU, *J. Reinf. Plastics Compos.* **9** (1990) 59.
5. A. F. KREGERS and G. A. TETERS, *Mech. Compos. Mater.* **17** (1981) 25.
6. C. YALVAC and TATISTCHEFF, *J. Reinf. Plastics Compos.* **8** (1989) 472.
7. C. D. RUDD, M. J. OWEN and V. MIDDLETON, *Compos. Sci. Technol.* **39** (1990) 261.
8. W. S. KUO and T. W. CHOU, *J. Am. Ceram. Soc.* **78** (1995) 783.
9. B. V. SHANKAR and R. V. MARREY, *Compos. Sci. Technol.* **49** (1993) 61.
10. J. D. WHITCOMB, "Composite Materials Fatigue and Fracture", ASTM STP 1110 (American Society for Testing and Materials, Philadelphia, PA, 1991).
11. K. WOO and J. B. WHITCOMB, *Commun. Numer. Methods Eng.* **9** (1993) 937.
12. C. C. CHAO, T. P. TUNG, C. C. SHEU and J. H. TSENG, *J. Vibr. Acoust.* **116** (1994) 371.
13. W. S. KUO and T. W. CHOU, in "Proceedings of 6th Technical Conference of American Society for Composites" (Technomic, Lancaster, 1991) p. 611.
14. *Idem*, *Ceram. Eng. Sci. Proc.* **12** (1991) 1556.
15. H. P. CHEN and B. Z. JANG, *Polym. Compos.* **16** (1995) 125.
16. S. RAMAKRISHNA and D. HULL, *Compos. Sci. Technol.* **50** (1994) 249.
17. W. S. KUO, in "Proceedings of the ICCM-10 Conference", Vol. 4, edited by A. Poursartip and K. Street (Woodhead, Cambridge, 1995) p. 301.
18. W. S. KUO and T. W. CHOU, *J. Am. Ceram. Soc.* **78** (1995) 745.
19. W. S. KUO and H. I. CHEN, *Compos. Sci. Technol.*, (in press) 1997.

Received 25 March 1996
and accepted 17 April 1997